

Series-Resonant Matrix Inverter with Asymmetrical Modulation for Improved Power Factor Correction in Flexible Induction Heating Appliances

Pablo Guillén, *Student Member, IEEE*, Héctor Sarnago, *Senior Member, IEEE*, Óscar Lucía, *Senior Member, IEEE*, and José M. Burdío, *Senior Member, IEEE*

Post Conference Paper

Abstract—Induction heating appliance operation is constrained by the non-linear pot material behavior under the generated magnetic field. The equivalent load seen by the inverter varies with the intensity of the field, meaning that this variation is dependent on the mains voltage. In flexible-surface induction cooktops, this fact is combined with a high coil number and different pots to be powered simultaneously, increasing the complexity to control the transmitted power while maintaining proper mains current consumption. In this paper, two non-complementary asymmetrical modulations with in-cycle parameter variation are proposed for improved power factor correction while avoiding the need for switching frequency variation and intermodulation noise in multi-load systems. The proposed strategies are analyzed and experimentally tested using a 3.6 kW multi-inverter prototype featuring 5 induction coils.

Index Terms— Asymmetrical modulations, home appliances, induction heating, multiple output, power control, resonant inverters.

I. INTRODUCTION

INDUCTION heating (IH) has increased its relevance as a heating technology due to its numerous advantages such as fast heating, safe and clean operation, and high efficiency [1]. Most of these advantages are a consequence of generating the heat directly on the target material, which is done by means of two mechanisms: eddy currents and magnetic hysteresis [1-4]. In order to induce both effects, a medium frequency magnetic field has to be applied to the material (Fig. 1 (a)).

The material penetration depth, $\delta = 1/\sqrt{\pi f \mu_r \sigma}$, changes with the frequency, f , conductivity, σ , and material

This work was supported in part by the Spanish MICINN and AEI under Project PID2019-103939RB-I00 and Project PDC2021-120898-I00, co-funded by EU through FEDER and NextGenerationEU/PRTR programs, by the DGA-FSE, by the MCIU under the FPU grant FPU17/01442, and by the BSH Home Appliances Group.

P. Guillén, H. Sarnago, O. Lucía and J. M. Burdío are with the Department of Electronic Engineering and Communications, I3A, University of Zaragoza, Zaragoza, 50018, Spain (P. Guillén phone: +34 876555318; e-mail: pguillenm@unizar.es).

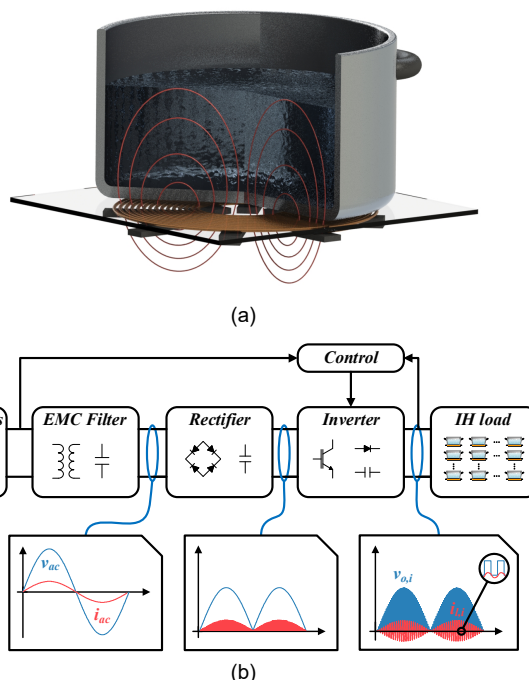


Fig. 1. Induction heating load in domestic application composed by the induction coil and the pot (a), and a typical multi-output induction cooktop block diagram (b).

permeability, μ_r , that is dependent on the magnetic flux, ϕ , meaning that it is not constant but varies with the coil current [5]. Considering a typical home appliance implementation, as the depicted in Fig. 1 (b), this current depends, among other factors, on the voltage applied to the IH load by means of the inverter, which equals the rectified mains voltage if the bus capacitor value is low enough. As a consequence, the penetration depth fluctuates along the mains cycle and, consequently, the IH load seen by the inverter varies [6].

In Fig. 2, the changes in the IH load for different applied voltages and under different conditions of temperature and switching frequency can be seen. In this figure, the induction heating load is represented by its equivalent parameters: an equivalent series inductance, L_r , and an equivalent series

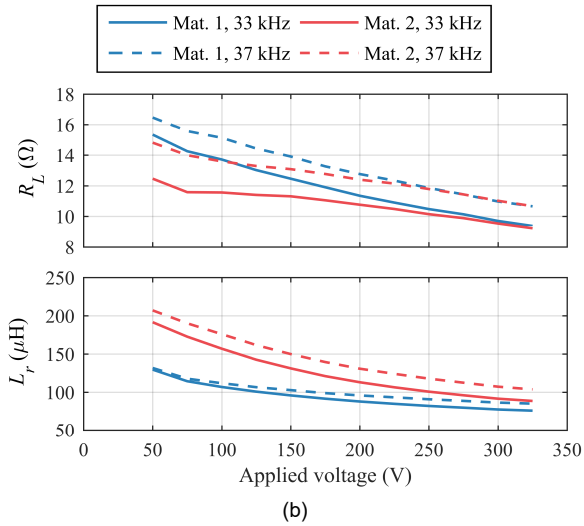
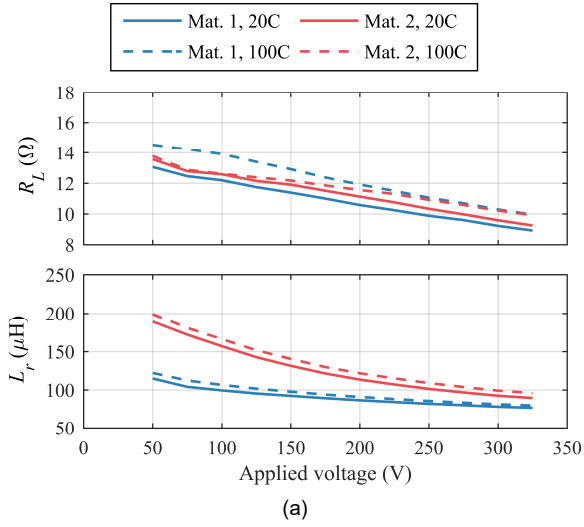


Fig. 2. Equivalent load parameter fluctuation under various applied voltages at different temperatures and constant frequency of 35 kHz (a) and different switching frequencies and constant temperature of 100 C (b).

resistance, R_L [7-9]. The main consequence of this is the change in the equivalent inverter resistance seen from the mains, $R_{ac,eq}$, which is depicted in Fig. 3. As a result, the mains current, i_{ac} , which is inversely proportional, increases near the mains peak, leading to third harmonic presence and increased total harmonic distortion (THD). Besides, the current is lower in the zero crossing vicinity, limiting the bus capacitor discharge and therefore degrading the power factor (PF). An example of the increase in the harmonic contribution can be seen in Fig. 4, where the mains voltage, v_{ac} , is also represented as a sinusoidal reference.

This issue is a major concern in induction cooktops as they have to fulfill electromagnetic compatibility regulations [10] while enabling the final user to use the desired pot regardless its non-linear behavior. A typical solution considered in the literature relies in using a low value bus capacitor that allows high power factor with a cost-effective implementation [11-15], which can be complemented by applying a frequency

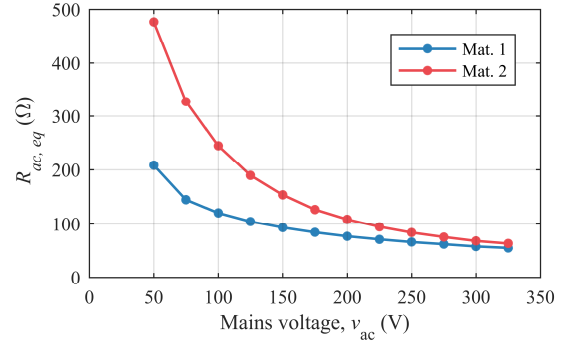


Fig. 3. Equivalent resistance as seen from the mains, $R_{ac,eq}$, for the full mains voltage range and two different pot materials at 100 C and the inverter operating at 35kHz.

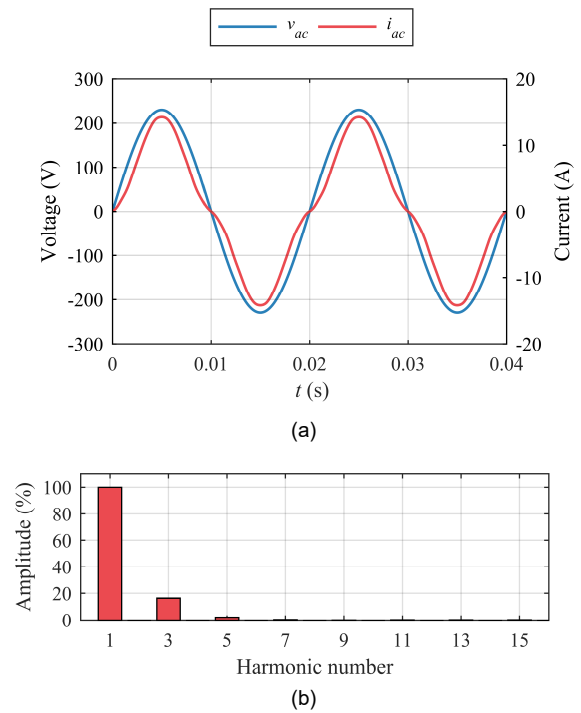


Fig. 4. Mains voltage and mains current example with Material 1 (a) and harmonic components of the mains current (b).

sweep to compensate the aforementioned THD [16-20]. Additionally, in order to improve the PFC capabilities of these applications, several topologies have been proposed in the literature to integrate the PFC stage in the inverter [21-28]. However, the increase of cooktop flexibility aggravates the problem [29, 30], as the presence of different pots differently coupled usually leads to intermodulation noise if different switching frequencies are present. Consequently, it is usually required the addition of an external PFC stage [31-36]. This is especially relevant when operating in multi-output converters that present limitations in the flexibility of control parameters.

In the past, in order to achieve proper output power control while avoiding the switching frequency limitation, constant-frequency asymmetrical modulations with offline calculation of the parameter profile have been proposed [37].

In order to generalize this solution, this paper proposes the usage of two non-complementary asymmetrical modulations

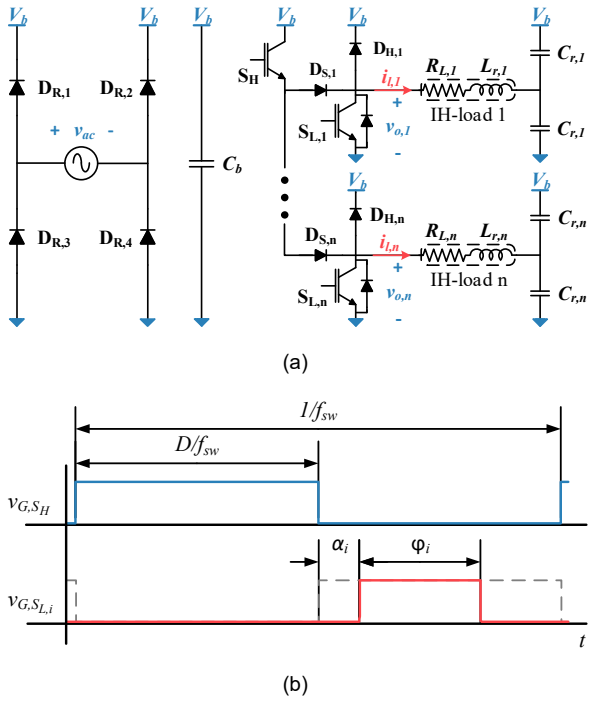


Fig. 5. Series-resonant matrix inverter topology (a) and modulation control parameters (b).

with in-cycle parameter variation to reduce the current distortion and improve power factor while controlling the transmitted power and operating with fixed frequency. Compared with previous proposals, this modulation strategy enables power factor correction without requiring an additional PFC stage. The proposed strategies are analyzed and experimentally tested using a 3.6 kW multi-output prototype.

The remainder of this paper is organized as follows: Section II presents the power converter topology under study and the power control capabilities with the asymmetrical modulation. Section III proposes the in-cycle parameter variation strategy and analyzes its implications in power and harmonic control. Section IV presents the proposed algorithm, and some simulation results and Section V presents the experimental setup and summarizes the main experimental results. Finally, Section VI draws the main conclusions of the paper.

II. PROPOSED POWER CONVERTER TOPOLOGY

A. Multi-Output ZVS Inverter Topology

The proposed converter is a single column variant derived from the multi-output matrix ZVS resonant inverter [38, 39]. This implementation presents a high-side transistor common to all IH loads, which are organized in rows.

The proposed topology is depicted in Fig. 5 (a), including the rectifier bridge, DR,1-4, and the bus capacitor, Cb. As previously discussed, the high side transistor, SH, is shared by all the IH load while each one is presented in a different output cell. These cells are comprised by the semiconductor devices, the IH load, and a split capacitor, Cr,i, to complete the resonant tank. The power devices are a high side antiparallel diode, DL,i, a low-side transistor, SL,i, with a built-in

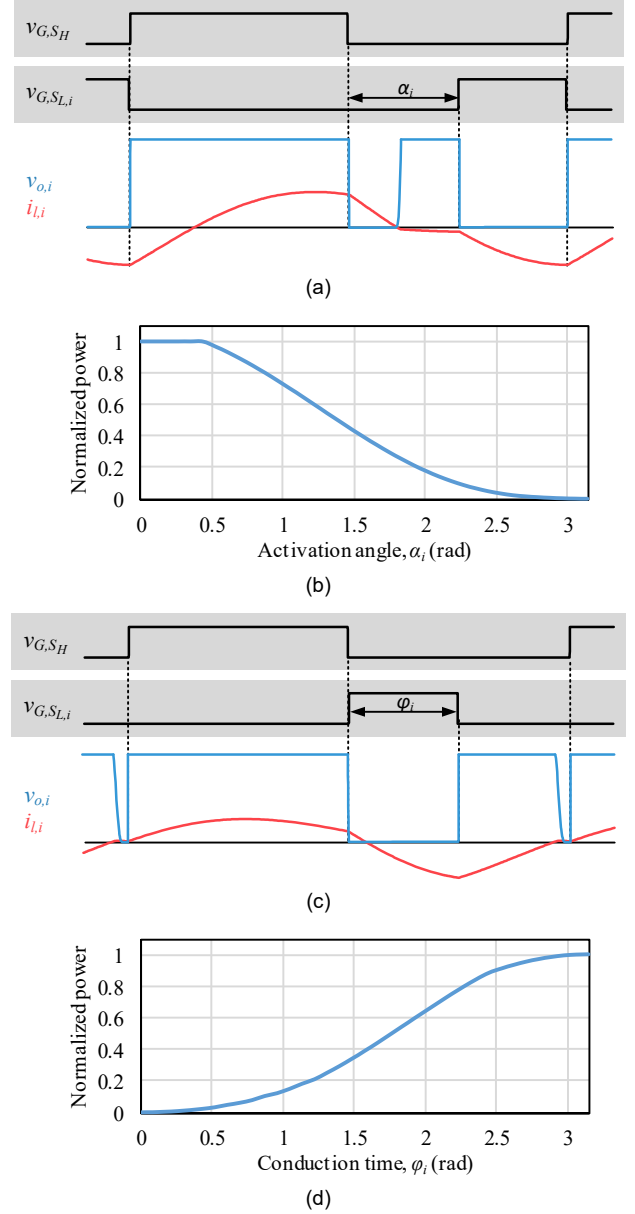


Fig. 6. Asymmetrical modulations for power factor correction: (a), Non-complementary pulse delay control (NC-PDC) and (c), Non-complementary pulse width modulation (NC-PWM), and power control capability of the NC-PDC (b) and NC-PWM (d) strategies.

antiparallel diode, DL,i, and a series diode, DS,i, that connects the cell with the high-side transistor.

The series diode allows the independent activation of each one of the cells. When the low side transistor is not activated in a switching period, the capacitor is charged and as a consequence, the series diode is reverse biased, so no power transmission occurs. However, if the transistor is activated, it generates a path to discharge the resonant capacitor, operating the branch similarly to the half bridge inverter, and ensuring that the series diode is forward biased when SH is activated.

B. Asymmetrical Non-Complementary Control Strategies

The active loads of the converter operate with modulation strategies similar to the ones used to operate the half-bridge

series resonant inverter. However, as it is shown in Fig. 5 (b), the common high side transistor, S_H , of this inverter forces equal switching frequency, f_{sw} , and duty cycle, D , for all branches. As a consequence, independent power control of the different IH loads is obtained by controlling the low-side transistor activation parameters allowing increased flexibility in the power transmission.

In Fig. 6, the two alternatives of non-complementary asymmetrical modulations with single parameter operation are shown: Non-complementary pulse delay control (NC-PDC), when the parameter that varies is α_i , and non-complementary pulse width modulation (NC-PWM) [40], varying the parameter φ_i . Both allow full-range power control, being the maximum power the transmitted with square waveform modulation, i.e. lowest α_i (Fig. 6 (b)) or highest φ_i (Fig. 6 (d)):

$$P_{o,i}(v_{ac}, f_{sw}, \alpha_i, \varphi_i) < P_{o,i}(v_{ac}, f_{sw}, 0, \pi). \quad (1)$$

Given that each inverter branch equivalent resistance as seen from the mains, $R_{ac,eq,i}$, can be defined as

$$R_{ac,eq,i}(v_{ac}) = \frac{V_{ac,rms}^2}{P_{o,i}(v_{ac}, f_{sw}, \alpha_i, \varphi_i)}, \quad (2)$$

the independent power control enables to set the desired total equivalent resistance of the complete inverter, $R_{ac,eq}$, as it can be approximated as the parallelization of all branches.

Additionally, the independent power control modulation strategies allow different equi-resistance operation for the different IH loads and thus different power transmission.

III. MAINS CURRENT CONTROL

The mains current, i_{ac} , can be described as

$$i_{ac}(t) = \frac{\hat{V}_{ac}}{R_{ac,eq}(v_{ac})} \sin(2\pi f_{ac} t), \quad (3)$$

where f_{ac} is the mains frequency. Therefore, the desired sinusoidal current, $i_{ac,obj}$, is achieved by maintaining a constant $R_{ac,eq}$, independently of the voltage fluctuation, which is denoted as $R_{ac,obj}$. Considering equations (1) and (2), it is important to note that correction is possible when $R_{ac,eq}$ is lower than $R_{ac,obj}$, i.e. i_{ac} is higher than the desired $i_{ac,obj}$.

In Fig. 7, the originally distorted mains current, i_{ac} , is presented in comparison a $i_{ac,obj}$ curve corresponding with the desired $R_{ac,obj}$. This figure shows the mains period fraction where correction is possible, t_{sin} . Thus, the resulting non-distorted current, $i_{ac,nd}$, can be expressed as

$$i_{ac,nd}(t) = \begin{cases} i_{ac}(t) & t \leq \frac{1}{4f_{ac}} - \frac{t_{sin}}{2} \\ \frac{\hat{V}_{ac}}{R_{ac,obj}} \sin(2\pi f_{ac} t) & \frac{1}{4f_{ac}} - \frac{t_{sin}}{2} < t \leq \frac{1}{4f_{ac}} + \frac{t_{sin}}{2} \\ i_{ac}(t) & t > \frac{1}{4f_{ac}} + \frac{t_{sin}}{2} \end{cases}, \quad (4)$$

where

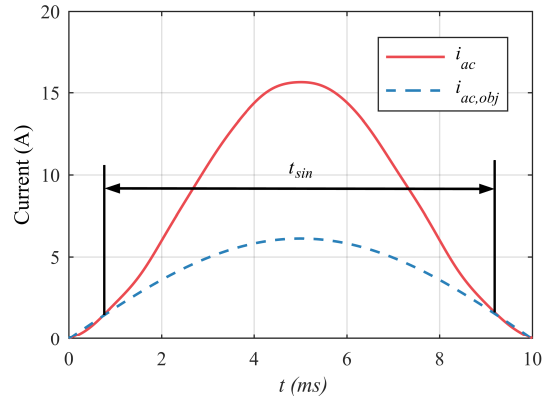


Fig. 7. Comparison between the original distorted current, i_{ac} , and the desired sinusoidal current, $i_{ac,obj}$, which corresponds with a constant $R_{ac,obj}$.

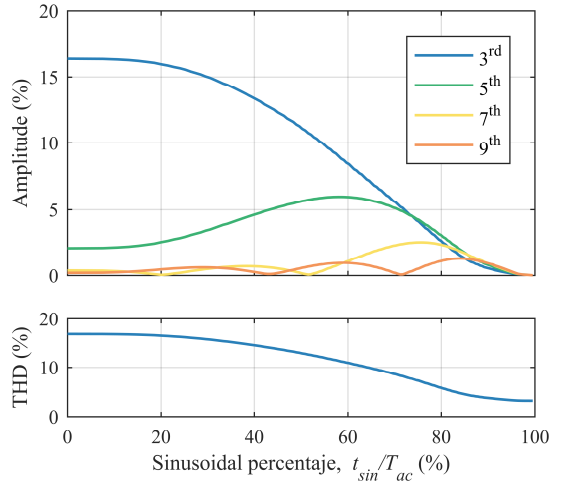


Fig. 8. Harmonic component variation depending on the i_{sin} share of the total period.

$$t_{sin} = t \Big|_{R_{ac,eq}(v_{ac}) < R_{ac,obj} = (\hat{V}_{ac}/\sqrt{2})^2 / P_{o,obj}}. \quad (5)$$

Consequently, the sinusoidal part of the current decreases with the increase of the desired transmitted power, $P_{o,obj}$. As a consequence, in order to maximize t_{sin} , $R_{ac,eq}$ can be reduced by approximating the switching frequency close to the resonant frequency while maintaining ZVS commutation. A comparison of the achieved THD reduction as a function of t_{sin} can be seen in Fig. 8.

A. Proposed in-cycle parameter variation

To achieve the desired constant $R_{ac,obj}$, the control parameter has to adapt the load $R_{L,i}$ and $L_{r,i}$ variation. Analytically, the different $R_{ac,eq,i}$ as a function of the control parameter can be derived from equation (2). For the case of the NC-PDC strategy, it can be calculated as shown in equation (6), being $t_{0,\alpha}$ the current zero crossing time, that depends on the load parameters. This parameter can be approximated as

$$R_{ac,\alpha_i}(v_{ac}) = \frac{1}{R_{L,i}(v_{ac}) \left(\sum_{h=1}^H \frac{(\sin(h\alpha_i) - \sin(ht_{0,\alpha_i}(v_{ac})))^2 + (1+(-1)^h (\cos(ht_{0,\alpha_i}(v_{ac})) - \cos(h\alpha_i) - 1))^2}{(h\pi)^2 (R_{L,i}^2(v_{ac}) + (h\omega_s L_{r,i}(v_{ac}) - (1/h\omega_s C_{r,i}))^2)} \right)}, \quad (6)$$

$$R_{ac,\varphi_i}(v_{ac}) = \frac{1}{R_{L,i}(v_{ac}) \left(\sum_{h=1}^H \frac{((\sin(ht_{0,\varphi_i}(v_{ac})) - \sin(h\varphi_i))^2 + (-\cos(ht_{0,\varphi_i}(v_{ac})) + \cos(h\varphi_i) - 1 + (-1)^h)^2)}{(h\pi)^2 (R_{L,i}^2(v_{ac}) + (h\omega_s L_{r,i}(v_{ac}) - (1/h\omega_s C_{r,i}))^2)} \right)}, \quad (8)$$

$$t_{0,\alpha_i}(v_{ac}) = \tan^{-1} \left(\frac{\omega_s h L_{r,i}(v_{ac}) - \frac{1}{\omega_s h C_r}}{R_{L,i}(v_{ac})} \right). \quad (7)$$

For the NC-PWC strategy, the equivalent resistance is calculated in equation (8) being in this case $t_{0,\varphi}$ equal to

$$t_{0,\varphi_i}(v_{ac}) = \tan^{-1} \left(\frac{\sin(\varphi_i) R_{L,i}(v_{ac}) + (-1 + \cos(\varphi_i)) \left(\omega_s L_{r,i}(v_{ac}) - \frac{1}{\omega_s C_r} \right)}{(-1 + \cos(\varphi_i)) R_{L,i}(v_{ac}) - \sin(\varphi_i) \left(\omega_s L_{r,i}(v_{ac}) - \frac{1}{\omega_s C_r} \right)} \right). \quad (9)$$

The curves for various levels of $R_{ac,obj}$ and the two pot materials can be compared in Fig. 9. In this figure, differences in the voltage range that allow parameter change can be seen, corresponding with the differences on t_{sin} as calculated in (5).

B. Transmitted power control

The selection of the $R_{ac,obj,i}$ depends on the power that is desired to transmit to each load. The total transmitted power to the load, $P_{o,i}$, is calculated during a mains cycle as

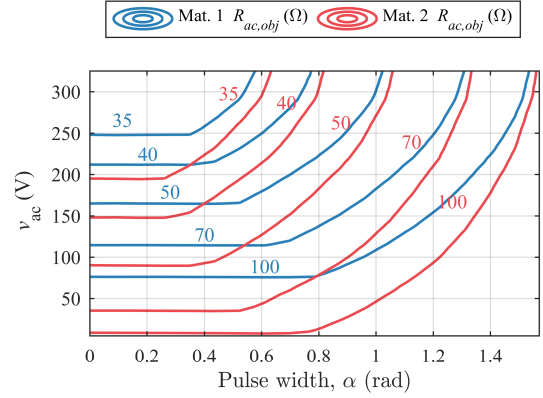
$$P_{o,i} = f_{ac} \int_0^{\frac{1}{f_{ac}}} \frac{(\hat{V}_{ac} \sin(2\pi f_{ac} t))^2}{R_{ac,eq,i}(v_{ac})} dt, \quad (10)$$

and the objective equivalent resistance can be estimated substituting the desired power, $P_{o,obj,i}$, in equation (2) as

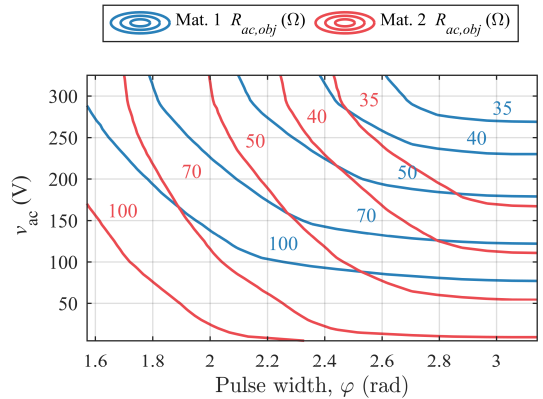
$$R_{ac,obj,i} = \frac{\hat{V}_{ac}^2}{P_{o,obj,i}}. \quad (11)$$

However, the controlled transmitted power corresponds only with the sinusoidal part of the current

$$P_{cntr,i} = 2f_{ac} \int_{\frac{1}{4f_{ac}}}^{\frac{1}{4f_{ac}} + \frac{t_{sin}}{2}} \frac{(\hat{V}_{ac} \sin(2\pi f_{ac} t))^2}{R_{ac,obj,i}} dt = \frac{\hat{V}_{ac}^2 (\sin(2\pi f_{ac} t_{sin}) + 2\pi f_{ac} t_{sin})}{R_{ac,obj,i}}, \quad (12)$$



(a)



(b)

Fig. 9. Equal resistance curves for two pot materials operating the inverter at the same f_{sw} and with the non-complementary pulse delay control (NC-PDC) strategy (a), and the non-complementary pulse width modulation (NC-PWM) strategy (b).

meaning that the mains cycle power should be measured and $R_{ac,obj,i}$ modified accordingly.

IV. CONTROL ALGORITHM

The proposed control system can be seen in Fig. 10. It is divided into two main blocks: branch equivalent resistance recalculation, and branch constant resistance control. This structure, achieves the power factor correction with a precise control in the transferred power. The first block operates at the

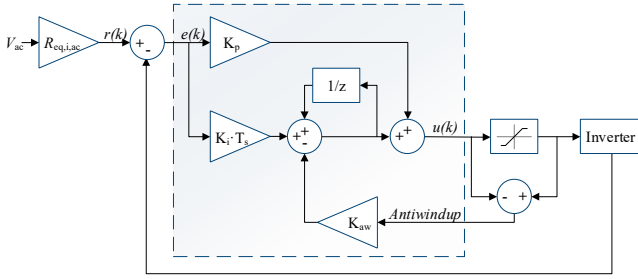


Fig. 10. Control block schematic.

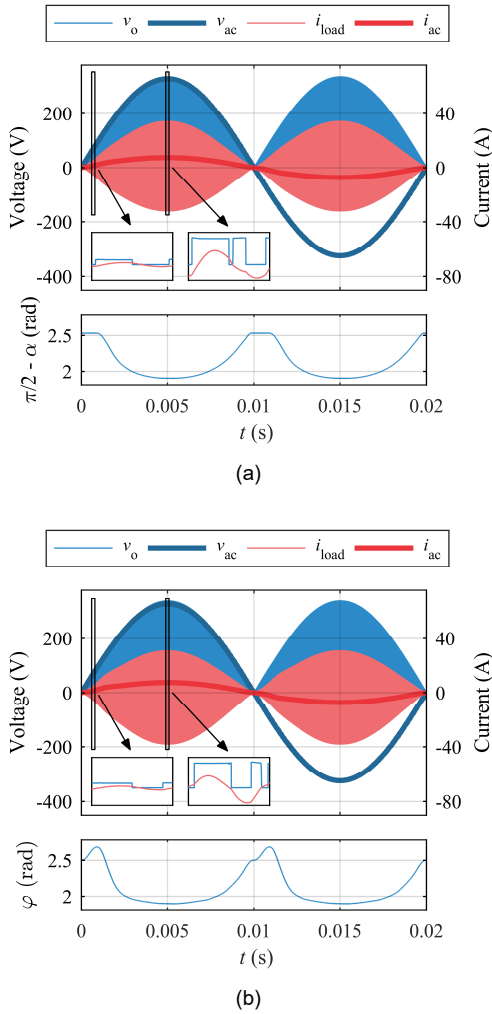


Fig. 11. Asymmetrical modulations for power factor correction: Non-complementary pulse delay control (NC-PDC) (a) and Non-complementary pulse width modulation (NC-PWM) (b).

mains frequency, f_{ac} , while the second one operates at switching frequency.

The $R_{ac,obj,i}$ recalculation part operates by calculating the difference between the real transmitted power to the load, $P_{o,i}$, and the expected power, $P_{o,obj,i}$ and then including the error in equation (11).

The constant resistance control is comprised by a PI controller with an anti-windup block. The latter is necessary as

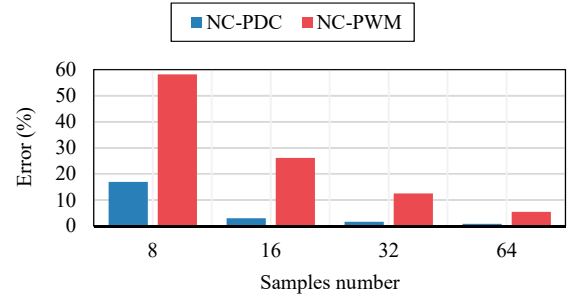


Fig. 12. Power calculation variation depending on the sampling rate for both modulation strategies.

the action variation, i.e. α or φ parameter, is limited for both



Fig. 13. Experimental test-bench including the IH coils, the pot, the power electronics prototype and the oscilloscope to capture the converter waveforms.

modulation strategies. Between 0 and π radians for the case of φ , and between the diode conduction time and π for the variation of parameter α .

A. Simulation results

Simulation results for the algorithm with both parameter variations and a single load are shown in Fig. 11. Both alternatives present and appropriate THD reduction of approximately the 70%. Additionally, in both simulations, it is important to note the asymmetrical parameter variation, as the PI controller also compensates the incomplete bus capacitor discharge.

However, the feasibility of the results is highly dependent of the power calculation and, as a result of the voltage and current waveforms, the sampling frequency. In Fig. 12, the power calculation error when the sampling instant is close to the low side transistor turn on is shown. As it can be seen, it is always more critical for the case of NC-PWM as the low side transistor switches in the current peak, discouraging its experimental implementation.

V. EXPERIMENTAL SETUP AND RESULTS

The experimental setup is presented in Fig. 13. A flexible surface comprised by an array of oval-shaped IH coils is used, allowing the free placement of the pot. The AC power source correspond with the California Instruments 5001 iX, that allow a power of up to 5 kW per phase and direct analysis of the current quality. Additional waveform measurements are obtained using the Teledyne Lecroy MDA810 oscilloscope. The measurement setup shown corresponds with: mains

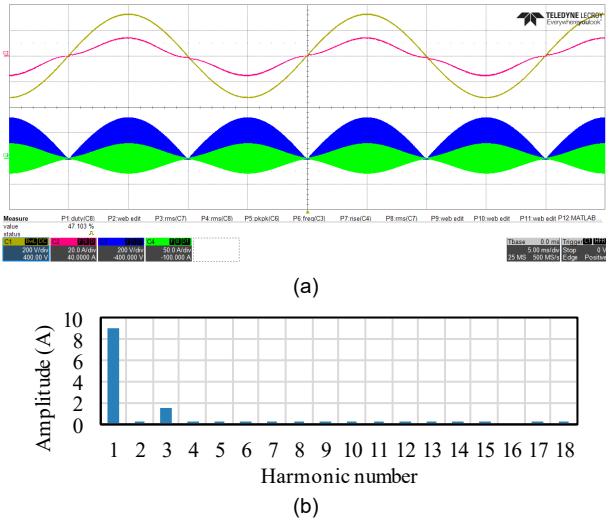


Fig. 14. Experimental results of the cooktop operating at nominal power with a highly non-linear pot and without PFC modulation. Main waveforms (a) and harmonic contribution (b). On the oscilloscope capture, from top to bottom: mains voltage, v_{ac} , (200 V/div, yellow), mains current, i_{ac} , (20 A/div, pink), active loads output voltage, v_o , (200 V/div, blue), active loads current, i_i , (50 A/div, green). Time axis: 5 ms/div.

current, i_{ac} , and voltage, v_{ac} , and single load applied voltage, $v_{o,i}$ and current, $i_{l,i}$. The converter prototype has been purposefully designed to allow the verification of the NC-PDC modulation strategy and integrates both the power topology and the control ancillary circuitry.

The multi-output inverter presents a single high-side transistor and 5 low-side branches. The transistors are IHW40N65R5S from Infineon and are selected to be the same considering that the maximum converter rated power is 3600 W, while each of the loads provide up to 2000 W independently. The selected diodes are APT30D60BHBG, from Microchip which provide good performance while allowing integrating D_S and D_H in the same TO-247-3 package. A forced-air cooling heatsink is used to achieve good power dissipation. Each one of the IH coil is commercial and the resonance has been designed following the commercial standards of induction cooktops.

The platform allows measuring the relevant parameters such as each branch applied voltage, $v_{o,i}$ and load current, $i_{l,i}$, to calculate the transmitted power, and the neutral and line voltages in order to be synchronized with the mains. In order to do so, 1 MSPS ADC converters have been used, ensuring low power calculation error. Based on that data, it is possible to apply the proposed modulation strategies by means of an embedded Spartan-6 XC6SLX9 FPGA in which the proposed algorithm has been implemented.

Additionally, the platform includes optic-fiber connections that allow its connection with an external PC that runs the user interface and provides the prototype with each load desired power level.

A. Experimental results

In Fig. 14, the mains and load waveforms for a non-controlled constant-frequency power transmission are shown for a highly non-linear material, i.e. Material 1. The transmitted power equals 2000 W and it is shared between two

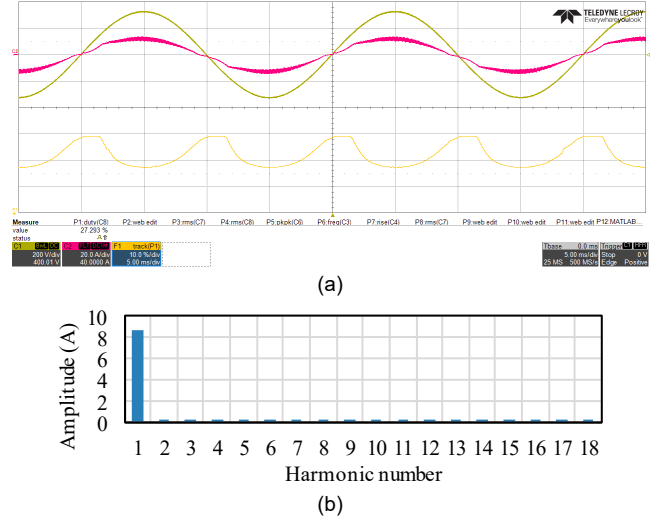


Fig. 15. Experimental results of the cooktop operating at nominal power with NC-PDC PFC modulation and a highly non-linear pot. Main waveforms (a) and harmonic contribution (b). In (a), from top to bottom: mains voltage, v_{ac} , (200 V/div, yellow), mains current, i_{ac} , (20 A/div, pink), low side transistor active time percentage, $50\%-\alpha$, (10 %/div, dark yellow). Time axis: 5 ms/div.

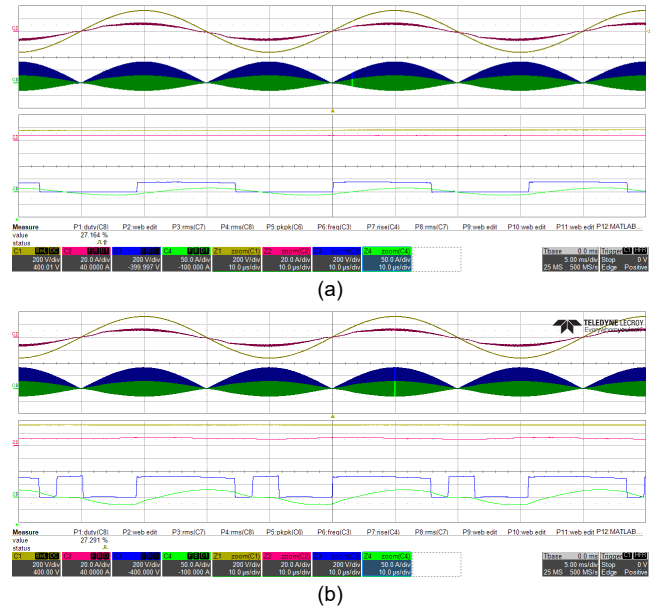


Fig. 16. Detailed waveforms of the cooktop operating at nominal power with NC-PDC PFC modulation and a highly non-linear pot. Zoom near the zero crossing (a) and the mains peak (b). On each capture, from top to bottom: mains voltage, v_{ac} , (200 V/div, yellow), mains current, i_{ac} , (20 A/div, pink), active loads output voltage, v_o , (200 V/div, blue), active loads current, i_i , (50 A/div, green). Time axis: 5 ms/div, 10 μs/div.

IH loads. As it can be seen, the current waveform presents a significant 3rd harmonic component, which corresponds with the $R_{ac,eq}$ variation along the mains cycle, high asymmetry, due to the uneven bus capacitor charge and discharge, and zero crossing distortion. In Fig. 14 (b), the RMS values of the harmonic components of the current, are shown. Additionally, more relevant data measured by the power analyzer has been transcribed to Table I.

TABLE I. PF, THD, AND HARMONIC CONTENT WITH AND WITHOUT THE PROPOSED MODULATION.

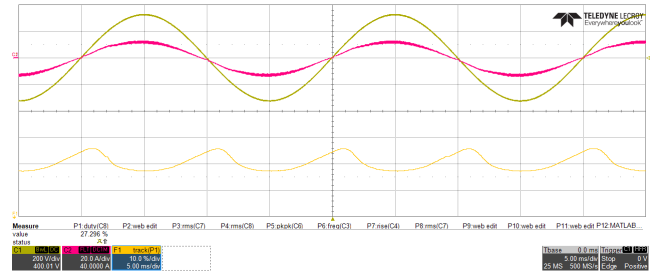
	MATERIAL 1			MATERIAL 2		
	2000 W No-PFC MODULATION	2000 W NC-PDC PFC MODULATION	3000 W NC-PDC PFC MODULATION	2000 W No-PFC MODULATION	2000 W NC-PDC PFC MODULATION	3000 W NC-PDC PFC MODULATION
PF	0.984	0.992	0.991	0.995	0.994	0.997
THD (%)	16.18	4.58	10.83	6.77	2.28	3.30
Harmonic content	Normalized value (%)	Normalized value (%)	Normalized value (%)	Normalized value (%)	Normalized value (%)	Normalized value (%)
Fundamental	100	100	100	100	100	100
2	0.16	0.16	0.17	0.15	0.14	0.10
3	16.21	0.89	8.60	6.67	0.62	2.13
4	0.04	0.10	0.04	0.02	0.12	0.02
5	2.05	2.59	6.27	0.78	1.31	1.81
6	0.01	0.07	0.03	0.02	0.12	0.05
7	0.36	2.73	1.91	0.12	1.16	1.35
8	0.02	0.07	0.03	0.02	0.03	0.01
9	0.16	1.96	0.81	0.14	0.70	0.73
10	0.02	0.22	0.02	0.01	0.05	0.01

In contrast with the previous results, the usage of the proposed NC-PDC modulation strategy under the same conditions as the reference measurement, i.e. Material 1 and 2000 W, can be seen in Fig. 15. There, voltage and current are represented as well as the control parameter fluctuation along the mains cycle. The α variation profile reduces i_{ac} in the vicinity of the mains peak and due to its asymmetry is capable of compensating the mismatch between V_b and $|v_{ac}|$. By doing this, a reduction of the 3rd harmonic can be seen in Fig. 15 (b) and the improvement of the PF is summarized in Table I.

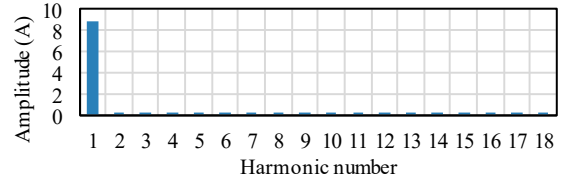
The α parameter variation effect over the IH load waveforms can be seen in Fig. 16. There, square waveform operation occurs near the zero crossing when $i_{ac,obj} \geq i_{ac}$ and therefore α is lower than $t_{0,\alpha}$ (Fig. 16 (a)) and high non-complementarity occurs near the mains peak (Fig. 16 (b)).

The experimental results for a material with a less pronounced non-linear behavior, i.e. Material 2, can be seen in Fig. 17. There, a similar parameter profile is obtained but with a reduced α variation range.

In Table I, the most relevant experimental data considering different power levels is summarized. PF improvements and THD reductions can be seen when using NC-PDC PFC modulation. Additionally, the main harmonic components of the presented waveforms are shown as a percentage of the fundamental harmonic in order to allow a proper comparison. The dependency of the power factor correction capability with the relation between $i_{ac,obj}$ and i_{ac} can be seen, since the results



(c)



(d)

Fig. 17. Experimental results of the cooktop operating at nominal power with NC-PDC PFC modulation and a non-linear pot. Main waveforms (a) and harmonic contribution (b). In (a), from top to bottom: mains voltage, v_{ac} , (200 V/div, yellow), mains current, i_{ac} , (20 A/div, pink), low side transistor active time percentage, 50%- α , (10 %/div, dark yellow). Time axis: 5 ms/div.

improve for lower power values as $i_{ac,obj}$ decreases and the sinusoidal percentage increases.

TABLE II. IEC 61000 3 2:2018 COMPARISON FOR MAXIMUM POWER WITH AND WITHOUT THE PROPOSED MODULATION.

HARMONIC CONTENT	MATERIAL 1				MATERIAL 2			
	No-PFC MODULATION	% OF LIMIT	NC-PDC PFC MODULATION	% OF LIMIT	No-PFC MODULATION	% OF LIMIT	NC-PDC PFC MODULATION	% OF LIMIT
Fundamental	15.654		15.683		15.744		15.637	
3	2.662	115.72	0.531	23.10	1.249	54.32	0.100	4.34
5	0.326	28.58	0.659	57.82	0.138	12.15	0.158	13.88
7	0.075	9.79	0.404	52.41	0.032	4.10	0.122	15.89
9	0.038	9.38	0.167	41.67	0.027	6.79	0.095	23.71
2	0.049	4.55	0.037	3.46	0.032	2.97	0.043	3.99
4	0.052	12.10	0.129	30.01	0.034	7.87	0.031	7.29
6	0.049	16.40	0.121	40.25	0.031	10.44	0.043	14.27
8	0.045	19.42	0.017	7.53	0.029	12.51	0.049	21.38
10	0.024	12.85	0.030	16.21	0.024	12.88	0.016	8.63

Additionally, in Table II the proposed modulations are compared according to the standard IEC 61000 3 2:2018 with a 300-mm pot placed sharing three induction coils and maximum rated power. In this test, the improvement achieved with the highly non-linear pot is clearly highlighted as it allows the converter to fit below the harmonic limits.

VI. CONCLUSIONS

In this paper, a matrix ZVS resonant power converter and two non-complementary pulse modulation strategies with in-cycle parameter variation have been proposed as single stage PFC and THD reduction solution for flexible surface cooktops. Closed loop control has been proposed to achieve load adaptation and smooth control parameter fluctuation.

The NC-PDC has been validated experimentally due to the lower error derived from the power calculation. For a highly non-linear material it achieves a PFC of 0.07 points and a THD reduction of an 80% by addressing the 3rd harmonic component excess. The proposed algorithm has been tested in a multi-output prototype with an embedded FPGA and the simulation results have been experimentally validated, proving the applicability of the proposed modulation strategies to a prototype operating under real operating conditions.

REFERENCES

- [1] O. Lucía, P. Maussion, E. Dede, and J. M. Burdío, "Induction heating technology and its applications: Past developments, current technology, and future challenges," *IEEE Transactions on Industrial Electronics*, vol. 61, pp. 2509-2520, May 2014.
- [2] J. Davies, *Conduction and Induction heating*. London: Peter Peregrinus Ltd., 1990.
- [3] A. Mühlbauer, *History of Induction Heating and Melting*. Essen: Vulkan-Verlag GmbH, 2008.
- [4] V. Rudnev, D. Loveless, R. Cook, and M. Black, *Handbook of induction heating*. New York: Marcel Dekker Inc., 2003.
- [5] J. Serrano, J. Acero, I. Lope, C. Carretero, J. M. Burdío, and R. Alonso, "Modeling of domestic induction heating systems with non-linear saturable loads," in *2017 IEEE Applied Power Electronics Conference and Exposition (APEC)*, 2017, pp. 3127-3133.
- [6] J. Villa, L. A. Barragan, J. I. Artigas, D. Navarro, A. D. Vicente, and T. Cabeza, "SoC-based In-Cycle Load Identification of Induction Heating Appliances," *IEEE Transactions on Industrial Electronics*, pp. 1-1, 2020.
- [7] O. Jiménez, O. Lucía, I. Urriza, L. A. Barragán, and D. Navarro, "Analysis and implementation of FPGA-based online parametric identification algorithms for resonant power converters," *IEEE Transactions on Industrial Informatics*, vol. 10, pp. 1144-1153, May 2014.
- [8] C. Carretero, O. Lucía, J. Acero, R. Alonso, and J. M. Burdío, "Frequency-dependent modeling of domestic induction heating systems using numerical methods for accurate time-domain simulation," *IET Power Electronics*, vol. 5, pp. 1291-1297, September 2012.
- [9] H. Sarnago, O. Lucía, and J. M. Burdío, "A Versatile Resonant Tank Identification Methodology for Induction Heating Systems," *IEEE Transactions on Power Electronics*, vol. 33, pp. 1897-1901, Mar 2018.
- [10] IEC, "IEC 61000-3-2:2018 Electromagnetic compatibility (EMC) - Part 3-2: Limits - Limits for harmonic current emissions (equipment input current ≤ 16 A per phase)."
- [11] H. Fujita and H. Akagi, "Pulse-density-modulated power control of a 4 kW, 450 kHz voltage-source inverter for induction melting applications," *IEEE Transactions on Industry Applications*, vol. 32, pp. 279-286, 1996.
- [12] R. Ordóñez and H. Calleja, "Induction heating inverter with power factor correction," in *6th IEEE Power Electronics Congress. Technical Proceedings. CIEP 98 (Cat. No.98TH8375)*, 1998, pp. 90-95.
- [13] S. Wang, K. Izaki, I. Hirota, H. Yamashita, H. Omori, and M. Nakaoka, "Induction-heated cooking appliance using new quasi-resonant ZVS-PWM inverter with power factor correction," *IEEE Transactions on Industry Applications*, vol. 34, pp. 705-712, 1998.
- [14] R. C. M. Gomes, M. A. Vitorino, D. A. Acevedo-Bueno, and M. B. R. Corrêa, "Three-Phase Integrated PFC AC-AC Resonant Inverter with Weak Coupled Coils for Induction Heating Application," in *2019 IEEE Energy Conversion Congress and Exposition (ECCE)*, 2019, pp. 5720-5725.
- [15] S. Hisayuki, M. Sang-Pil, K. Soon-Kurl, M. Tomokazu, and N. Mutsuo, "High-frequency resonant matrix converter using one-chip reverse blocking IGBT-Based bidirectional switches for induction heating," in *2008 IEEE Power Electronics Specialists Conference*, 2008, pp. 3960-3966.
- [16] J. Villa, A. Dominguez, L. A. B. Perez, J. I. Artigas, J. Espanol, and D. Navarro, "Conductance Control for Electromagnetic-Compatible Induction Heating Appliances," *IEEE Transactions on Power Electronics*, pp. 1-1, 2021.
- [17] L. A. Barragan, D. Navarro, J. Acero, I. Urriza, and J. M. Burdío, "FPGA Implementation of a Switching Frequency Modulation Circuit for EMI Reduction in Resonant Inverters for Induction Heating Appliances," *IEEE Transactions on Industrial Electronics*, vol. 55, pp. 11-20, 2008.
- [18] A. Sandali, A. Cheriti, P. Sicard, and K. Al-Haddad, "Application of PDM control to a multilevel AC/AC converter with self power factor correction," in *2004 IEEE 35th Annual Power Electronics Specialists Conference (IEEE Cat. No.04CH37551)*, 2004, pp. 2881-2887 Vol.4.
- [19] A. Sandali, A. Cheriti, and P. Sicard, "PDM Ac/ac converter with three-phase diode rectifier including power factor correction," in *2008 IEEE International Symposium on Industrial Electronics*, 2008, pp. 347-352.
- [20] J. Villa, A. Domínguez, L. A. Barragán, J. I. Artigas, J. Español, and D. Navarro, "Conductance Control for Electromagnetic-Compatible Induction Heating Appliances," *IEEE Transactions on Power Electronics*, vol. 37, pp. 2909-2920, 2022.
- [21] T. Takahara, M. Okamoto, E. Hiraki, T. Tanaka, T. Hashizume, and T. Kachi, "Performance verification of a novel soft switching three-phase utility frequency AC to high frequency AC direct power converter with PFC function for industrial IH applications," in *Proceedings of 14th International Power Electronics and Motion Control Conference EPE-PEMC 2010*, 2010, pp. T6-54-T6-60.
- [22] T. Mishima, Y. Nakagawa, and M. Nakaoka, "A Bridgeless BHB ZVS-PWM AC-AC Converter for High-Frequency Induction Heating Applications," *IEEE Transactions on Industry Applications*, vol. 51, pp. 3304-3315, 2015.
- [23] S. Khatroth and P. Shunmugam, "Single-stage pulse frequency controlled AC-AC resonant converter for different material vessel induction cooking applications," *International Journal of Circuit Theory and Applications*, vol. 49, pp. 2865-2884, 2021.
- [24] N. A. Ahmed and M. Nakaoka, (2006, Boost-half-bridge edge resonant soft switching PWM high-frequency inverter for consumer induction heating appliances. *IEE Proceedings - Electric Power Applications* 153(6), 932-938.
- [25] B. Saha, S. K. Kwon, N. A. Ahmed, H. Omori, and M. Nakaoka, "Commercial Frequency AC to High Frequency AC Converter With Boost-Active Clamp Bridge Single Stage ZVS-PWM Inverter," *IEEE Transactions on Power Electronics*, vol. 23, pp. 412-419, 2008.
- [26] H. Sugimura, S. Kwon, H. Sadakata, S. Sumiyoshi, H. Omori, and M. Nakaoka, "Single stage series load resonant ZVS-PWM high frequency inverter operating at one diode conduction and critical ZCS PFC rectifier," in *2009 International Conference on Electrical Machines and Systems*, 2009, pp. 1-6.
- [27] S. Zenitani, M. Okamoto, E. Hiraki, and T. Tanaka, "A charge boost type multi output full bridge high frequency soft switching inverter for IH cooking appliance," in *Proceedings of 14th International Power Electronics and Motion Control Conference EPE-PEMC 2010*, 2010, pp. T2-127-T2-133.
- [28] N. A. Ahmed, "High-Frequency Soft-Switching AC Conversion Circuit With Dual-Mode PWM/PDM Control Strategy for High-Power IH Applications," *IEEE Transactions on Industrial Electronics*, vol. 58, pp. 1440-1448, 2011.
- [29] O. Lucía, J. Acero, C. Carretero, and J. M. Burdío, "Induction heating appliances: Towards more flexible cooking surfaces," *IEEE Industrial Electronics Magazine*, vol. 7, pp. 35-47, September 2013.

- [30] O. Lucía, H. Sarnago, and J. M. Burdío, "Soft-Stop Optimal Trajectory Control for Improved Performance of the Series Resonant Multi-Inverter for Domestic Induction Heating Applications," *IEEE Transactions on Industrial Electronics*, vol. 62, pp. 6251-6259, October 2015.
- [31] M. Pérez-Tarragona, H. Sarnago, O. Lucía, and J. M. Burdío, "Design and Experimental Analysis of PFC Rectifiers for Domestic Induction Heating Applications," *IEEE Transactions on Power Electronics*, vol. 33, pp. 6582-6594, 2018.
- [32] M. Pérez-Tarragona, H. Sarnago, O. Lucía, and J. M. Burdío, "A front-end PFC stage for improved performance of flexible induction heating appliances," *International Journal of Applied Electromagnetics and Mechanics*, vol. 63, pp. 115-121, 2020.
- [33] M. Pérez-Tarragona, H. Sarnago, J. M. Burdío, and O. Lucía, "Multi-Phase PFC Rectifier and Modulation Strategies for Domestic Induction Heating Applications," *IEEE Transactions on Industrial Electronics*, vol. 68, pp. 6424-6433, Dec 2021.
- [34] Y. Kawaguchi, E. Hiraki, T. Tanaka, H. Sadakata, A. Fujita, H. Omori, *et al.*, "A comparison of operation mode for soft-switching PFC converter for induction heating cooking appliance," in *Industrial Electronics, 2009. IECON '09. 35th Annual Conference of IEEE*, 2009, pp. 13-18.
- [35] Y. Kawaguchi, E. Hiraki, T. Tanaka, H. Sadakata, A. Fujita, H. Omori, *et al.*, "A comparative evaluation of DCM control and CCM control for soft-switching PFC converter," in *IECON 2010 - 36th Annual Conference on IEEE Industrial Electronics Society*, 2010, pp. 250-255.
- [36] H. Sugimura, B. Saha, S. Kwon, S. Hideki, S. Sumiyoshi, H. Omori, *et al.*, "A single stage induction heating high frequency series load resonant ZVS-PWM inverter with active filtering pfc rectifier operating at one diode conduction and ZCS commutation," in *2009 IEEE 6th International Power Electronics and Motion Control Conference*, 2009, pp. 689-695.
- [37] P. Guillén, H. Sarnago, L. Ó, and J. M. Burdío, "Power Factor Correction using Asymmetrical Modulation for Flexible Induction Heating Appliances," in *2021 IEEE Applied Power Electronics Conference and Exposition (APEC)*, 2021, pp. 753-757.
- [38] H. Sarnago, J. M. Burdío, and O. Lucía, "High Performance and Cost Effective ZCS Matrix Resonant Inverter for Total Active Surface Induction Heating Appliances," *IEEE Transactions on Power Electronics*, vol. 34, pp. 117-125, 2019.
- [39] P. Guillén, H. Sarnago, O. Lucía, and J. M. Burdío, "Mains-Synchronized Pulse Density Modulation Strategy Applied to a ZVS Resonant Matrix Inverter," *IEEE Transactions on Industrial Electronics*, pp. 10835-10844, Dec 2021.



Pablo Guillén (S'19) received the M.Sc. degree in Industrial Engineering from the University of Zaragoza, Zaragoza, Spain, in 2017.

During 2017, he held a research internship with the Bosch and Siemens Home Appliances Group. He is currently a Ph.D. Student with the Department of Electronic Engineering and Communications, the University of Zaragoza. His main research interests include resonant power converters and digital control applied to induction heating.

Mr. Guillen is a member of the Aragon Institute for Engineering Research (I3A).



Héctor Sarnago (S'09, M'15) received the M.Sc. degree in Electrical Engineering and the Ph.D. degree in Power Electronics from the University of Zaragoza, Spain, in 2010 and 2013, respectively.

Currently, he is a senior post-doc researcher in the Department of Electronic Engineering and Communications at the University of Zaragoza, Spain. His main research interests include resonant converters and digital control for induction heating applications.

Dr. Sarnago is a member of the Aragon Institute for Engineering Research (I3A).



Óscar Lucía (S'04, M'11, SM'14) received the M.Sc. and Ph.D. degrees (with honors) in Electrical Engineering from the University of Zaragoza, Spain, in 2006 and 2010, respectively.

During 2006 and 2007 he held a research internship at the Bosch and Siemens Home Appliances Group. Since 2008, he has been with the Department of Electronic Engineering and Communications at the University of Zaragoza, Spain, where he is currently an Associate

Professor with accreditation for Full Professor. He was a visiting scholar in the Center for Power Electronics Systems (CPES, Virginia Tech. USA) in 2009 and 2012, and the TU Berlin (Germany) in 2019. His main research interests include resonant power conversion, wide-bandgap devices, and digital control, mainly applied to wireless power transfer, induction heating, electric vehicles, and biomedical applications. In these topics, he has published more than 100 international journal papers and 170 conference papers, and he has filed 50 international patents.

Dr. Lucía is a Senior Member of the IEEE, and an active member of the Power Electronics (PELS) and Industrial Electronics (IES) societies. Currently, he is an Associate Editor of the IEEE Transactions on Industrial Electronics, the IEEE Transactions on Power Electronics, IEEE Industrial Electronics Magazine and the IEEE Open Journal of the Industrial Electronics Society. Dr. Lucía has received the 2020 IEEE Industrial Electronics Magazine Best Paper Award and the "Agustín de Betancourt y Molina" Award by the Real Academia de Ingeniería. Dr. Lucía is a member of the Aragon Institute for Engineering Research (I3A).



José M. Burdío (M'97, SM'12) received the M.Sc. and Ph.D. degrees in Electrical Engineering from the University of Zaragoza, Zaragoza, Spain, in 1991 and 1995, respectively.

He has been with the Department of Electronic Engineering and Communications, University of Zaragoza, where he is currently a Professor, the Head of the Group of Power Electronics and Microelectronics, and the Director of the BSH Power Electronics Laboratory at the University of Zaragoza. He is the author of more than 80 international journal papers and over 200 conference papers, and the holder of more than 60 international patents. His main research interests include modeling of switching converters and resonant power conversion for induction heating and biomedical applications.

Dr. Burdío is a senior member of the IEEE and the Power Electronics and Industrial Electronics Societies. He is also a member of the Aragon Institute for Engineering Research (I3A).